



1 Neural network modelling to estimate particle size distribution 2 based on other particle sections and meteorological parameters

3 Pak Lun Fung^{1,2}, Martha Arbayani Zaidan^{1,3}, Ola Surakhi⁴, Sasu Tarkoma⁵, Tuukka Petäjä^{1,3} and
4 Tareq Hussein^{1,6,7}

5 ¹Institute for Atmospheric and Earth System Research / Physics, Faculty of Science, University of Helsinki, Finland;
6 pak.fung@helsinki.fi; martha.zaidan@helsinki.fi; tuukka.petaja@helsinki.fi; tareq.hussein@helsinki.fi

7 ²Helsinki Institute of Sustainability Science, Faculty of Science, University of Helsinki, Finland

8 ³Joint International Research Laboratory of Atmospheric and Earth System Sciences, School of Atmospheric Sciences, Nanjing
9 University, Nanjing 210023, China

10 ⁴Department of Computer Science, The University of Jordan, Amman 11942, Jordan; ola.surakhi@gmail.com

11 ⁵Department of Computer Science, Faculty of Science, University of Helsinki, Finland; sasu.tarkoma@helsinki.fi

12 ⁶Department Material Analysis and Indoor Chemistry, Fraunhofer WKI, D-38108 Braunschweig, Germany

13 ⁷Department of Physics, The University of Jordan, Amman 11942, Jordan

14 *Correspondence to:* Pak Lun Fung and Tareq Hussein

15 Abstract.

16 In air quality research, often only particle mass concentrations as indicators of aerosol particles are considered. However,
17 the mass concentrations do not provide sufficient information to convey the full story of fractionated size distribution,
18 which are able to deposit differently on respiratory system and cause various harm. Aerosol size distribution
19 measurements rely on a variety of techniques to classify the aerosol size and measure the size distribution. From the raw
20 data the ambient size distribution is determined utilising a suite of inversion algorithms. However, the inversion problem
21 is quite often ill-posed and challenging to invert. Due to the instrumental insufficiency and inversion limitations, models
22 for fractionated particle size distribution are of great significance to fill the missing gaps or negative values. The study at
23 hand involves a merged particle size distribution, from a scanning mobility particle sizer (NanoSMPS) and an optical
24 particle sizer (OPS) covering the aerosol size distributions from 0.01 to 0.42 μm (electrical mobility equivalent size) and
25 0.3 μm to 10 μm (optical equivalent size) and meteorological parameters collected at an urban background region in
26 Amman, Jordan in the period of 1st Aug 2016–31st July 2017. We develop and evaluate feed-forward neural network
27 (FFNN) models to estimate number concentrations at particular size bin with (1) meteorological parameters, (2) number
28 concentration at other size bins, and (3) both of the above as input variables. Two layers with 10–15 neurons are found to
29 be the optimal option. Lower model performance is observed at the lower edge ($0.01 < D_p < 0.02 \mu\text{m}$), the mid-range
30 region ($0.15 < D_p < 0.5 \mu\text{m}$) and the upper edge ($6 < D_p < 10 \mu\text{m}$). For the edges at both ends, the number of neighbouring
31 size bins is limited and the detection efficiency by the corresponding instruments is lower compared to the other size bins.
32 A distinct performance drop over the overlapping mid-range region is due to the deficiency of a merging algorithm.
33 Another plausible reason for the poorer performance for finer particles is that they are more effectively removed from the
34 atmosphere compared to the coarser particles so that the relationships between the input variables and the small particles
35 is more dynamic. An observable overestimation is also found in early morning for ultrafine particles followed by a distinct
36 underestimation before midday. In the winter, due to a possible sensor drift and interference artefacts, the model
37 performance is not as good as the other seasons. The model by meteorological parameters using 5-min data ($R^2 = 0.22$ –
38 0.58) shows poorer results than data with longer time resolution ($R^2 = 0.66$ – 0.77). The model by the number concentration
39 at the other size bins can serve as an alternative way to replace negative number in size distribution raw dataset thanks to



40 its high accuracy and reliability ($R^2 = 0.97-1$). This negative numbers filling method can maintain a symmetric
41 distribution of errors.

42

43 **Keywords.**

44 Aerosol size distribution, feed-forward neural network, atmospheric aerosols particles, missing data; SMPS; OPS

45 **1 Introduction**

46 Particulate matter (PM) is the principal component of air pollution. PM includes a range of particle sizes, such as coarse
47 ($1 < D_p < 10 \mu\text{m}$), fine ($0.1 < D_p < 1 \mu\text{m}$), and ultrafine particles (UFP, $D_p < 0.1 \mu\text{m}$). Through human's inhalation, coarse
48 particles usually are partly deposited in the head airway ($5-30 \mu\text{m}$) by the inertial impaction mechanism, and are partly
49 deposited in the tracheobronchial region, mainly through sedimentation ($1-5 \mu\text{m}$). The particles may be further absorbed
50 or removed by mucociliary clearance (Gupta and Xie, 2018). The remaining fine and UFP, due to their high surface area
51 to mass ratios (Kreyling et al., 2004), penetrate deeply into the alveolar region, where removal mechanisms may be
52 insufficient (Gupta and Xie, 2018). Evidence suggests that the adverse associations of short-term UFP exposure with
53 acute and chronic problems ranging from inflammation, exacerbation of asthma, and metal fume fever to fibrosis, chronic
54 inflammatory lung diseases, and carcinogenesis (Spinazzè et al., 2017) might be at least partly independent of other
55 pollutants (Ohlwein et al., 2019). Various studies have demonstrated that inhaled or injected UPF could enter systemic
56 circulation and migrate to different organs and tissues (Xing et al., 2016; Londahl et al., 2014).

57

58 Other than health effects, particles of various sizes also contribute to Earth's ecosystem and climate differently. For
59 instance, fine and UFP are capable of growing up to diameters of $0.02-0.1 \mu\text{m}$ within a day (Kulmala et al.,
60 2004; Kerminen et al., 2018) where they constitute a fraction of cloud condensation nuclei, and thus, indirectly affecting
61 the climate (Kerminen et al., 2012). The drivers behind aerosol particles vary between natural and anthropogenic as well
62 as primary and secondary. Primary particles are emitted to the atmosphere as particles, such as sea salt or dust particles,
63 while secondary particles form in the atmosphere through gas-to-particle transformation, which has been known as new
64 particle formation (NPF) observed in various environments and contributing to a major fraction of the total particle
65 number budget (Kulmala et al., 2004; Kerminen et al., 2018). In addition, while fine particles cool the climate by
66 predominantly scattering shortwave radiation, coarse particles warm the climate system by absorbing both shortwave and
67 longwave radiation (Kok et al., 2017). Indeed, the complexity of urban aerosols is tribute to the fact that several sources
68 can contribute in the same particle size range (Rönkkö et al., 2017).

69

70 Currently, the most commonly reported aerosol variables are particle mass concentration and particle number
71 concentration. The former metric, which is dominated by coarser particles, is included as air quality indicators (e.g. mass
72 concentrations of both thoracic particles PM_{10} and fine particles $\text{PM}_{2.5}$); however, it has been argued that this might ignore
73 the potential adverse effect of UFP on health (Zhou et al., 2020). The latter one describes better the distribution of finer
74 particles, but it neglects the influence of coarse particles. Using either particle mass concentration or particle number
75 concentration solely is not enough to fully review the health effects and the Earth's climate system by aerosol particles.
76 Therefore, in order to understand the origin of atmospheric aerosol particles and their potential impacts at a specific
77 location, the whole size distribution of these particles needs to be studied (Zhou et al., 2020).

78



79 Recently, due to urbanization and increased population, megacities have increased their contribution to atmospheric
80 aerosol pollution massively Lelieveld et al. (2015). Middle East and North Africa (MENA) regions, with an average
81 annual growth rate of 1.74% in 2019 (World Bank Group, 2019), has one of the world's regions most rapidly expanding
82 populations. With the population of 578 million, several cities in MENA regions are among the 20 most polluted cities in
83 the world. The annual average concentrations of some pollutants, for example PM_{2.5} in MENA (54.0 µg m⁻³) often exceed
84 5 times the WHO recommended levels (10.0 µg m⁻³) (World Health Organisation, 2019). Many countries in MENA are
85 dealing with negative impacts of air pollution in terms of both economic burden and health aspect (Ahmed et al.,
86 2017;Goudarzi et al., 2019). Air Pollution in this region is estimated to cause 133,000 premature deaths annually, almost
87 half of which are attributed to natural sources of air pollution, such as windblown sea salt and desert dust (Gherboudj et
88 al., 2017). Apart from natural pollutants, anthropogenic activities also play a major role in driving the air quality. They
89 include the extensive development of petrochemical industry, vehicular emissions and open burning of waste (Arhami et
90 al., 2018).

91

92 However, aerosol studies in this region have not paid attention to the aerosol number size distribution so far. Among the
93 few studies published, most report mass concentration (Goudarzi et al., 2019;Arhami et al., 2018;Borgie et al., 2016),
94 while some focused on the total particle number in MENA regions. Studies on the size-fractionated number concentrations
95 are, nonetheless, scarce (e.g. Hakala et al., 2019) due to the unavailability of instruments for measuring UFP in many air
96 quality monitoring stations (Spinazzè et al., 2017). Determining aerosol number size distribution for a wide size range in
97 a reliable manner is a challenging task. The fact that the ambient distributions range from nanometers to several
98 micrometers dictates the use of multiple sizing techniques. For the sub-micron size range, electrical mobility equivalent
99 diameter is commonly used as the size parameter and the measurements are performed with Differential Mobility Particle
100 Sizer (DMPS) or Scanning Mobility Particle Sizer (SMPS) instruments (e.g. Wiedensohler et al., 2012). These systems
101 determine the aerosol size according to electrical mobility equivalent size. The larger particles (approximately > 0.3 µm)
102 can be classified according to their aerodynamic or optical size (Kulkarni et al., 2011). In order to obtain the full aerosol
103 size distribution, this data needs to be merged. Unfortunately this task is not trivial as the merging requires knowledge on
104 the chemical composition (influencing the refractive index and thus the optical size), shape (influencing electrical mobility
105 equivalent size), or effective density (influencing aerodynamic size) (Kannosto et al., 2008).

106

107 In addition, the raw data from these instruments must be inverted to obtain the particle size distribution. This is not a
108 straightforward problem. A proper inversion algorithm is required to restore the particle size distribution using the
109 recorded kernel function between the raw response and the size distribution (Cai et al., 2018). Depending on the
110 instruments used and the measurement environments, some use a built-in inversion algorithm in the instruments. Some
111 develop their own inversion methods; however, they all have their drawbacks. Examples include that the least square
112 method may magnify the random errors in CPC raw counts into relatively large uncertainties (Enting and Newsam, 1990),
113 the stepwise method may cause non-negligible errors (Lehtipalo et al., 2014), and that the smoothing step method may
114 introduce bias in the shape of the inverted distribution function. (Markowski, 1987). Kandlikar and Ramachandran (1999)
115 pointed out that there is not a single universal inversion algorithm applicable to all situations.

116

117 In this study, the built-in inversion algorithm was used. Especially in the size range of low number concentration, this
118 algorithm can lead to negative values when the kernel functions are not optimally configured. These negative values have



119 no physical meanings. Some might just omit the negative values or simply use nearest neighbour linear interpolation to
120 replace the negative values. However, the former method might cause asymmetric error for very small measured number
121 concentration values (Viskari et al., 2012), while the latter could result in too high values concurrently. To fill this
122 knowledge gap, statistical models can serve as an alternative to estimate of size-fractioned number concentration by using
123 other available measurements.

124

125 Similar to other air quality parameters, modelling of size-fractionated particle number concentrations have been
126 increasingly brought into the spotlight because of its potential health hazards. One of the most commonly used data-
127 driven methods, generalised linear regression models, have been extensively utilised in modelling size-fractionated
128 particle number concentrations, for example, in urban regions in Helsinki, Finland (Clifford et al., 2011; Hussein et al.,
129 2007), in Toronto, Canada (Sabaliauskas et al., 2012), in Brisbane, Australia (Rahman et al., 2017), and in three cities in
130 Germany (Gerling et al., 2020). Besides linear regression models Mølgaard et al. (2013), refined the statistical model
131 using Bayesian inference and autoregressive parameters in five European cities Reggente et al. (2014) improvised by
132 Gaussian process based on the measurements of oxides of nitrogen in Antwerp, Belgium. These approaches are
133 categorised as transparent machine learning (ML) processes, as known as white-box (WB) models, from which one can
134 clearly explain how they behave, how they produce predictions and what the influencing variables are (Rudin, 2019).
135 Another data-driven approach black-box (BB) models, which refer to ML systems being viewed in terms of its inputs and
136 outputs, without any knowledge of its internal workings or underlying principles (Rudin, 2019). They are considered to
137 work generally better in terms of accuracy, but provide limited transparency and accountability regarding the results
138 (Zaidan et al., 2019; Fung et al., 2020). One example of BB model is artificial neural network (ANN), which were applied
139 extensively to estimate other air pollutant parameters (Freeman et al., 2018; Cabaneros et al., 2019). They provide a robust
140 approach for approximating complex functions due to its ability to mimic non-linearity of the functions and its well-
141 developed optimisation. Al-Dabbous et al. (2017) has demonstrated the use of ANN to estimate three ranges of UPF at a
142 roadside site in Fahaheel, Kuwait. They addressed the importance of including meteorological parameters in the modelling
143 process, which was later validated by Zaidan et al. (2020) who estimated daily and hourly total particle number
144 concentration by only a combination of meteorological parameters in Amman, Jordan.

145

146 The objectives of the paper is estimate aerosol total number concentration from meteorological observations and to
147 advance the previous study by Zaidan et al. (2020) with a finer temporal and size-bin resolution. In order to do so, we
148 place emphasis on to estimate particle number concentration of a specific size bin by the interaction with other size bins
149 and meteorological variables. In this study, we propose three approaches in terms of different input variables when we
150 carry out the modelling: (1) only meteorological parameters, (2) only particle size distribution, and (3) both particle size
151 distribution and meteorological parameters. Based on the general data analysis of the particle size distribution and the
152 meteorological condition, we further explain the source of different size bins at certain weather conditions and the
153 correlation among the particle size distribution and meteorological parameters in Section 3. Evaluation of models is
154 discussed in Section 4, in terms of its diurnal cycle, weekend effect and seasonal variation. We also examine the possible
155 technical reasons for the pattern found and the application of the models.



156 2 Methods

157 2.1 Measurement sites and Instruments

158 In this study, we collected a dataset obtained from a measurement campaign in Amman, the capital city of Jordan, between
159 1 August 2016 and 31 July 2017. The city represents an area with Middle Eastern urban conditions within the Middle
160 East and North Africa (MENA) region. This region serves as a compilation of different aerosol particle sources including
161 natural dust, anthropogenic pollution (e.g., generated from the petrochemical industry and urbanization), as well as new
162 particle formation.

163
164 The database includes particle size distribution and meteorological parameters, as mentioned in the first step in Figure 1.
165 The aerosol measurement was carried out at the aerosol laboratory located on the third floor of the Department of Physics,
166 University of Jordan (32°00' N, 35°52' E) in the neighbourhood of Al Jubeiha. The campus is situated at an urban
167 background region in northern Amman. In particular, the campaign measured the particle number size distribution using
168 a scanning mobility particle sizer (NanoScan SMPS 3910, TSI, MN, USA). It monitors the particle size distributions as
169 electrical equivalent diameter 0.01–0.42 μm (13 channels). The size range of the SMPS system can be extended to coarse
170 particles with an additional compact instrument: an optical particle sizer (OPS 3330, TSI, MN, USA). OPS measures
171 optical diameter 0.3–10 μm (13 channels). This optical sizing method reports an optical particle diameter, which is often
172 different from the electrical mobility diameter measured by the SMPS technique. The measurements were combined to
173 provide a particle size distribution of wider particle diameter range 0.01–10 μm , which is further described in Section 2.2.
174 The SMPS inlet flow rate was 0.75 lpm ($\pm 20\%$) while the sample flow rate was 0.25 lpm ($\pm 10\%$). The flow rate of OPS
175 was about 1 lpm. The aerosol transport efficiency through the aerosol inlet assembly was determined experimentally:
176 ambient aerosol sampling alternatively with and without sampling inlet, and the aerosol data was corrected accordingly.
177 The penetration efficiency was $\sim 47\%$ for 0.01 μm , $\sim 93\%$ for 0.3 μm and $\sim 40\%$ for 10 μm (Hussein et al., 2020). These
178 deficiency of measurement at the upper and lower edges is somewhat in alignment with other literatures. Particle size
179 measured by nanoSMPS (Tritscher et al., 2013) tended to be underestimated for spherical particles larger than 0.2 μm by
180 up to 34% (Fonseca et al., 2016). Liu et al. (2014) clearly portrayed that the detection limit of particle size below 0.03 μm
181 is about 80–500 cm^{-3} , which is up to 10 times larger than that of coarser particles, for other versions of SMPS. Stolzenburg
182 and McMurry (2018) explained that discrepancies could be resulted from DMAs with transfer functions that were
183 degraded (i.e., broadened) by flow distortions caused by particle deposition within the classifier tube, sizing errors due to
184 errors in flowmeter calibrations or leaks, CPC concentration errors due to improper pulse counting, and continuity failure
185 in the DMA high voltage connection.

186
187 The meteorological measurement was performed with a weather station (WH-1080, Clas Ohlson: Art.no.36-3242,
188 Helsinki, Finland) with a time resolution of 5 minutes. The meteorological data were comprised of ambient temperature
189 (Temp, resolution 0.1°C), relative humidity (RH, resolution 1%), wind speed (WS), wind direction (WD, 16 equal
190 divisions) and air pressure (P, resolution 0.3 hPa) (Hussein et al., 2019; Hussein et al., 2020; Zaidan et al., 2020). Wind
191 direction is resolved into north and east direction, as WD-N and WD-E, respectively. The data collection process is
192 illustrated in the first step in the database block in Figure 1.



193 2.2 Data pre-processing

194 The next step in Figure 1 is data pre-processing. Since the sampling time resolution of SMPS and OPS was 1 min and 5
195 min, respectively, we synchronised the data into 5-min average. Since a part of the size ranges in both instruments are
196 overlapping with each other, the last two size bins in SMPS and the first size bin in OPS were neglected. Finally, we
197 merged the size range of electrical mobility diameter 0.01–0.25 μm by SMPS and optical diameter 0.32–10 μm by OPS,
198 and obtain a wider particle size distribution which covers the diameter range 0.01–10 μm . Merging electrical mobility
199 diameter and optical diameter can be a challenge and the overlapping region is often calculated with high uncertainty
200 (DeCarlo et al., 2004; Tritscher et al., 2015). The challenge arises because the optical diameters are measured based on
201 the refractive index of the particles, which depends on their chemical composition. Therefore the sizing will vary over
202 time. There is also a very slight dependency with the SMPS system that is linked to the shape of the particles, which
203 influences their sizing.

204

205 We also calculated the particle number concentration with four particle diameter modes (size-fractionated number
206 concentration): nucleation (0.01–0.025 μm), Aitken (0.025–0.1 μm), accumulation (0.1–1 μm) and coarse mode (1–10
207 μm). Subsequently, the total number concentration was obtained as the sum of all these fractions. The size-fractionated
208 number concentrations were obtained by summing up the measured particle number size distribution over the specified
209 particle diameter range.

210

211 In order to perform neural network modelling, aerosol and meteorological data were first linearly interpolated in case of
212 short missing data periods. For missing data over longer periods, the whole rows are eliminated. The shorter missing data
213 occurs due to technical faults while the longer missing periods are attributed to instrument maintenance (Zaidan et al.,
214 2020). Only 71.8% of total data was retained for modelling in the measurement period. Since the data were obtained from
215 different measured variables with various physical units and magnitudes, it was crucial to normalise the data. The scaling
216 factor depends on which activation function is chosen. In this case, the datasets were scaled so that it has a mean of 0 and
217 a standard deviation of 1 to transform them into the range of the activation function. The standardised data was then
218 separated into different months for the reason of the seasonal variation in the atmospheric condition. The data was further
219 divided into training set (70%) and testing set (30%). The processed data were also converted to hourly and daily averages
220 for reporting purposes.

221 2.3 Modelling

222 After data collection and data pre-processing procedures, the next step is model optimisation (Figure 1). ANN models
223 have been utilised in predicting air quality (Freeman et al., 2018; Maleki et al., 2019; Cabaneros et al., 2019; Zaidan et al.,
224 2020). Neural networks provide a robust approach for approximating real-valued target functions because they can mimic
225 the non-linearity of the functions and their optimization methods are well developed (Zaidan et al., 2017). The architecture
226 of neural networks consists of nodes which generate a signal or remain silent as activation function (Figure 2). Activation
227 function in each layer determines the output value of each neuron that becomes the input values for neurons in the next
228 hidden layer connected to it. In this paper, feedforward neural network (FFNN) is used instead of a more sophisticated
229 time delay neural network (TDNN) because some of the rows in the dataset were removed in the data pre-processing step
230 due to the existence of missing data and TDNN cannot be performed without time continuity. FFNN usually consists of



231 a series of layers. The first layer has a connection from the network input. Each subsequent layer has a connection from
232 the previous layer. The final layer produces the network's output. A neuron can be thought as a combination of two parts:

$$z_j^{(L)} = \sigma\left(\sum_{i=1}^n w_{ji}^{(L)} x_i + b_j^{(L)}\right) \quad (1),$$

233 where $z_j^{(L)}$ and $b_j^{(L)}$ are the intermediate output and the bias term for the j^{th} neuron at L^{th} layer, respectively. $w_{ji}^{(L)}$ is the j^{th}
234 weight for each data points x_i at L^{th} layer. The second part performs the activation function (sigmoid function in this
235 study) on z_j to give out the output of the neuron:

$$\sigma(z_j^{(L)}) = \frac{1}{1 + \exp^{-z_j^{(L)}}} \quad (2),$$

236 The FFNN model was created, trained and simulated with MATLAB (version: 8.3.0.532), using Neural Network Toolbox.
237 We initialised the weights randomly and the weights are updated through "Levenberg-Marquardt" algorithm
238 optimisation that was the fastest available back-propagation training function (Chaloulakou et al., 2003). We performed
239 several iterations within a cycle to minimise the training loss with Bayesian regularisation. These steps were done
240 iteratively until the best combination of the number of hidden layers and the corresponding number of neurons that
241 provided the minimum error was found. According to the review paper by Cabaneros et al. (2019), a shallow neural
242 network with one hidden layer and enough neurons in the hidden layers can fit any finite input-output mapping problem
243 for non-linear relationship. In the network training process, the number of neurons varied from 2 to 10 neurons per layer
244 with an incremental factor of 2 neurons in each simulation, and from 10 to 25 per layer with an incremental factor of 5
245 neurons in each simulation. To keep the model simple, we consider only one or two layers in the simulation process
246 because the computing requirements could rise exponentially with the number of layers and neurons. Once we pick the
247 suitable model configuration, the model estimates number concentration using testing data. Finally, the selected
248 performance metrics, described in Section 2.4, can be calculated and we evaluate which approach is the most suitable for
249 size distribution estimation.

250 **2.4 Performance metrics**

251 We choose the optimal combination of the number of hidden layers and the corresponding number of neurons by checking
252 its mean absolute error (MAE), which is a simple way to illustrate the residuals of the estimated values by the model. In
253 order to identify which size bin manage to be predicted best, two metrics are used, namely coefficient of determination
254 (R^2) and normalised root-mean-square error (NRMSE). R^2 measures how well the observed outcomes are replicated by
255 the model, based on the proportion of total variation of outcomes explained by the model. NRMSE represents the standard
256 deviation of the estimated errors with respect to its mean. NRMSE is used rather than commonly used RMSE because the
257 number concentrations of the different size range are of different magnitudes. The comparison in different size range
258 becomes different if RMSE is not normalised with its mean.

$$\text{MAE} = \frac{\sum_{i=1}^n |y_i - \hat{y}_i|}{n} \quad (3)$$

$$R^2 = 1 - \frac{\sum_{i=1}^n (y_i - \hat{y}_i)^2}{\sum_{i=1}^n (y_i - \bar{y})^2} \quad (4)$$

$$\text{NRMSE} = \frac{\sqrt{\frac{\sum_{i=1}^n (y_i - \hat{y}_i)^2}{n}}}{\bar{y}} \quad (5)$$



259 where y_i , \hat{y}_i and \bar{y} represent the i^{th} measurement value, the y^{th} estimated value by the model and the mean of the all the
260 measurement data, respectively. n notates the total number of the valid measurement data.

261 **3 General data analysis**

262 **3.1 Environmental condition**

263 Hussein et al. (2019) and Zaidan et al. (2020) investigated and described the effect of local weather conditions,
264 respectively. Here we describe briefly the meteorological conditions during the measurement period as background
265 information. Starting from August 2016, the daily temperature decreased gradually from 40°C to its tough 0°C in February
266 2017. It rose gradually to 40°C in August 2017. During the measurement period, the hourly median value was 19.9°C
267 (Figure 3a). RH varied quite a lot from 10% to 100%, with an hourly median of 52.3%, and did not seem to have a
268 seasonal pattern (Figure 3b). In summer months, wind appeared be stronger but the wind direction is more stable, mostly
269 from northwest (270°–360°). In cold months, averaged wind speed was lower but wind blew from fluctuating direction.
270 During the whole measurement period, wind speed ranged between 0–6 m s⁻¹ and its median is 1.39 m s⁻¹ (Figure 3c,d).
271 Air pressure varied in a range from 892 to 912 hPa and its hourly median was 900 hPa In spite of the narrow range of
272 variation, winter months seem to have slightly higher air pressure than summer months (Figure 3e).

273
274 Meteorological conditions have been suggested to influence particle number concentration. Hussein et al. (2019)
275 demonstrated that number concentration had a rather complex relationship with temperature. Furthermore, number
276 concentration of submicron had a decreasing trend with respect to the wind speed which indicates that most of the
277 submicron fraction is originated from local sources such as combustion processes. Meanwhile, the number concentration
278 of coarse particles had higher concentrations at stagnant conditions and when the wind speed is higher than 5.5 m s⁻¹. It
279 is mainly because of road dust resuspension and might also be attributed to dust storm via long-range transport (Hussein
280 et al., 2019). In this study, we further explore how wind direction influences the particle number concentration (Figure
281 4). Wind coming from the northwest (225°–325°) was generally stronger, but lower particle number concentration was
282 detected because the measurement area is at the outskirts of downtown. Wind from East and South (45°–225°) has a lower
283 wind speed but a more intense hourly particle number concentration can be detected. From that direction situates the
284 urban city where all kinds of industrial activities take place. When considering only coarse particles, relatively high
285 number concentration is found when south-westerly wind is strong. This can further serve as an evidence that the source
286 of coarse particles in that region might come mostly from long range sea salt from Dead Sea or dust particles from nearby
287 deserts.

288 **3.2 General pattern of particle size distribution**

289 Hourly total number concentration ranged from $1.90 \times 10^3 \text{ cm}^{-3}$ to $1.52 \times 10^5 \text{ cm}^{-3}$ and its median was $1.36 \times 10^4 \text{ cm}^{-3}$. Figure
290 5a performed moderate seasonal pattern in general: lower in summer months and higher in colder months. Hussein et al.
291 (2019) also characterised the modal structure of the particle number size distribution for the same site. Four modes have
292 been detected by lognormal fitting, as known as DO-FIT algorithm and modal structure (Hussein et al., 2005; Hussein et
293 al., 2019), revealed that the mode number concentrations of the nucleation, Aitken, and coarse modes were lognormally
294 distributed around their geometric mean values: 0.022 μm , 0.062 μm , and 2.3 μm respectively. However, the accumulation
295 mode number concentration had two distinguished modes with particle diameter centred at 0.017 μm and 0.39 μm . As



296 seen in Table 1, the total number concentration of all particle size ($1.70 \pm 1.26 \times 10^4 \text{ cm}^{-3}$) is mostly accounted by Aitken
297 mode (45–80%, average: $1.09 \pm 1.01 \times 10^4 \text{ cm}^{-3}$), followed by nucleation mode (10–50%, average: $0.48 \pm 0.32 \times 10^4 \text{ cm}^{-3}$).
298 Accumulation mode (0–15%, average: $0.13 \pm 0.08 \text{ cm}^{-3}$) comes third and only less than 0.5% of the total particle number
299 concentration contain coarse particles with an average of $2.13 \pm 2.80 \text{ cm}^{-3}$ (Figure 5b-e). Seasonal pattern of the total
300 number concentration resembles the Aitken composition: lower proportion in summer months and higher in colder
301 months. The ratio of nucleation mode performs in an opposite way. The seasonal variation of total number concentration
302 is due to the more suppressed boundary layer in winter (Teinilä et al., 2019) and the elevated wood combustion (Hellén
303 et al., 2017). The particle number of accumulation and coarse mode steadily stay at a low proportion line, which did not
304 account for the total number concentration. It is also noticed that dust episodes occurred with the concentrations that often
305 exceeded 2 cm^{-3} and the daily concentration in the course of these episodes can rise to 20 cm^{-3} . These episodes were often
306 found in spring from February to May and some episodes can last for up to one week.

307

308 Similar to many other urban environments, the diurnal pattern observed in this study reflects the combustion emissions
309 from traffic activity, which is more during the workdays (Hussein et al., 2019). The two peaks of the nucleation mode
310 and Aitken mode in the cold months are relevant for the morning and the afternoon traffic rush hours, which are similar
311 to those noticed in most cities in other countries. In warmer months, the diurnal cycles are not as distinct, but a sharp peak
312 of nucleation mode around noon is found, which is associated with the occurrence of new particle formation. These events
313 occurred very often in the summer as suggested by Hussein et al. (2020). The amplitude of diurnal cycles of coarse mode
314 is small while the patterns of accumulation are not clear (Figure 6).

315 3.3 Correlation analysis

316 Figure 7 demonstrated the interaction among the whole measured spectrum shows three range clusters based on their
317 correlation with the number concentration at other bin sizes: 0.01–0.205 μm , 0.205–0.875 μm and 0.875–10 μm . 0.01–
318 0.205 μm and 0.875–10 μm fall entirely within the size range detected by SMPS and OPS, respectively. The 5-min number
319 concentration of smaller size and bigger size bins have clear and strong correlation with the concentration of its
320 neighbouring size bin. However, particles of size 0.205–0.875 μm are located in the overlapping regions by the two
321 instruments; as a result, do not correlate well with other size bins. The correlation of 5-min particle size distribution with
322 meteorological parameters are generally low. Temperature appears to be the most correlated parameters for all bin sizes
323 among all the parameters we used in this study. Smaller size range have higher Pearson's correlation coefficient (R) than
324 larger size range for WD, WS and P.

325

326 The 5-min averaged data show similar correlation for the particle size distribution except for the smallest size bin. The
327 hourly and daily data have higher correlation with the other size bins which are also monitored by SMPS. The 5-min
328 averaged data show different correlation from the hourly and daily averaged data performed by (Zaidan et al., 2020). The
329 correlations of 5-min size distribution with all meteorological variables are below 0.5 for all size range. However, for
330 hourly and daily averaged data, R is much higher in specific size bins. Hourly and daily temperature, in particular, show
331 increasing R with larger particle size for accumulation and coarse mode. Overall, the correlations increase with the longer
332 averaging windows. This might be due to the buffer period the meteorological conditions act on the dispersion of particles.
333 Based on this result, using data with finer temporal resolution might be considered to be less influential to the accuracy
334 of modelling.



335 4 Model Evaluation

336 4.1 General evaluation

337 Figure 8 illustrates how well the models of the three approaches perform in term of R^2 and NRMSE.

338 **Approach 1 (Size distribution prediction based on meteorological parameters only):** For more than half out of the
339 23 size bins, 2 layers and 15 neurons is the best combination where the residuals are the lowest (Table 2). Since the poor
340 correlation with meteorological condition, we expect a low correlation of determination even using the optimal
341 configuration neural network ($R^2 = 0.22$ – 0.58). The R^2 looks poor at the nucleation mode ($0.01 < D_p < 0.03 \mu\text{m}$) of the
342 whole size distribution around nucleation mode ($R^2 \sim 0.2$). The rest of the size bins have better and stable performance (R^2
343 $= 0.4$ – 0.58). This shows that the instrument might have a poor detection efficiency for particles of smaller size. By using
344 FFNN, the model performance of 5-min data for all size bins ($R^2 = 0.22$ – 0.58) is worse than using daily data ($R^2 = 0.77$)
345 performed in Zaidan et al. (2020). Compared with hourly data ($R^2 = 0.66$), the overall model performance of 5-min data
346 is comparable ($R^2 = 0.67$).

347 **Approach 2 (Mutual size distribution prediction based on other particle sections only):** work well with most
348 combination of number of layers and neurons. They did not show a clear difference among the combinations we choose.
349 There is no single combination which entirely outperform the others in all size bins. We summed up the MAE for all size
350 bins and decided to stick to 2 layers and 10 neurons with the overall lowest residuals (Table 2). R^2 are all above 0.97 for
351 all bin sizes, and NRMSE is 0.01–0.25 for bin sizes. The results are expected because there are 22 inputs and one output.
352 Relatively worse correlation at the edges of size bins ($0.01 < D_p < 0.02 \mu\text{m}$; $6 < D_p < 10 \mu\text{m}$) is found because of the lack
353 of nearby size bins which has high correlation with the corresponding size bin. Another reason could be that the instrument
354 has a higher detection limits for smaller particles (Liu et al., 2014). The poorer performance for smaller size might be due
355 to a coarser sizer resolution compared to other SMPS components (Tritscher et al., 2013), so that NanoSMPS does not
356 reflect the real enough size distribution in the atmosphere. Relatively poor modelling performance at the middle size range
357 ($0.15 < D_p < 0.5 \mu\text{m}$) in the whole measured spectrum is because of the overlapping of instruments. This also ascertain the
358 importance of creating a better algorithm when we merge two or more size distribution by different instruments. In this
359 study, the measuring techniques and the measuring targets are different by the SMPS and OPS. The merging of the two
360 measuring targets, the optical particle diameter and the electrical mobility diameter, might create significant uncertainties
361 (DeCarlo et al., 2004; Tritscher et al., 2015). The estimation of certain bin size by other bin sizes can be thought of
362 replacing negative values in the raw data by particle sizers. While some instrument manufactures create built-in algorithms
363 to replace with artificial non-negative numbers, most end-users simply remove the seemingly impossible negative values
364 from the dataset. The perfect way to do it is to have a parallel instrument that overlaps with that particle size range.
365 However, in many cases, this is not possible as a result of financial constraints. Therefore, we shall rely on the mutual
366 relationship between the size sections in the aerosol population. Negative values appear often at size bins with very low
367 number concentration (usually in coarse mode). Instead of eliminating them, this alternative could maintain the symmetry
368 of the error distribution of the number concentration (Viskari et al., 2012) and minimise the uncertainties caused.

369 **Approach 3 (Mutual size distribution prediction based on meteorological parameters and other particle sections):**
370 the general results are similar as in PSD. However, the more input variables do not enable the model to work better. At
371 some bin size the R^2 are even slightly smaller than PSD solely. Since meteorological data show low correlation with most
372 portion of measured spectrum. In that approach, the addition of meteorological parameters is not beneficial to the
373 modelling process. Due to the lack of improvement in the model development, we will only focus on the two models: met
374 and PSD from now on.



375

376 From the perspective of physics, particles in the nucleation mode ($0.01 < D_p < 0.03 \mu\text{m}$) are more sensitive to
377 transformation processes due to their volatility and rather unstable nature (Morawska et al., 2008). This leads to a
378 relatively short lifetime in the atmosphere (Al-Dabbous et al., 2017), therefore the relationships between the input
379 variables and the nucleation mode are not well established. Al-Dabbous et al. (2017) demonstrated that accumulation
380 mode particles ($0.1 < D_p < 0.3 \mu\text{m}$) have much longer lifetimes compared to smaller particles, causing them to be
381 transported for larger distances (Laakso et al., 2003); therefore, the mapping of the relationships between long-range
382 transported accumulation mode particles and covariates is supposed not to well understood. However, the relative
383 prediction ability in this study is not lower given that local meteorological variables were used as input variables. The
384 possible reason is that this mode falls exactly in the instrumental overlapping regions, which leads to a lower predictively.
385 The locally-produced Aitken mode particles ($0.03 < D_p < 0.1 \mu\text{m}$) are less effectively removed by transformation processes
386 (e.g., evaporation and coagulation) from the atmosphere, compared with nucleation mode ($0.01 < D_p < 0.03 \mu\text{m}$), allowing
387 the prediction models to better understand their relationships with the input variables, which is in alignment with Al-
388 Dabbous et al. (2017).

389 4.2 Temporal pattern

390 Figure 9 shows the diurnal discrepancies during workdays and weekends. Relative particle number concentration was
391 defined by the modelled concentration with respect to the measured concentration. Values above 1 indicates
392 overestimation while values below 1 suggests underestimation. For approach 1, except for the overlapping size bin, which
393 are underestimated by more than 50% at all time range, the difference between modelled and measured hourly number
394 concentration is within 50% during both workdays and weekends. Overestimation is found in early morning before 3 a.m.
395 during workdays for all size bins, especially for UFP. Following the overestimation, at about 6 a.m. in the morning, the
396 modelled number concentration appears to understate by up to 40%, especially at size bins below $0.1 \mu\text{m}$. Along the day,
397 the modelling uncertainties are rather small until in the evening from 6 p.m. to 11 p.m. where modelled UFP number
398 concentration show moderate overestimation one more time. It reveals that the model with only meteorological parameters
399 as inputs fail to catch the diurnal pattern from 6 p.m. to 7 a.m. in particular for UFP. The pattern of the performance for
400 weekends does not appear to be as distinctive as on workdays. It shows the overestimation not only for UFP in early
401 morning about 3 a.m., but also at the upper edge larger than $5 \mu\text{m}$ from 3 a.m. to 4 p.m.. At 7 p.m. onwards until noon, an
402 underestimation is found at all size bins. For approach 2, except the overlapping size bin, which has a significant
403 overestimation from 6 p.m. to 7 a.m., most show trivial 10% uncertainty during both workdays and weekends. The model
404 performance over weekends show relatively stronger uncertainties. The smallest bin at $0.01 \mu\text{m}$ is slightly understated for
405 all hours of a day. Other than these, models with the full spectrum of size distribution as inputs manage to catch fairly
406 well the diurnal pattern for all size bins.

407

408 Figure 10 further shows the monthly deviation in modelling performance. For approach 1, higher R^2 is found in November,
409 February and April in the range of SMPS. Other than that, no observable variation in R^2 in approach 1. For approach 2,
410 except in January when all the rows were eliminated because of the lack of wind information, performance in the other
411 months is steady for most size range. At $0.21 \mu\text{m}$, the difference in model performance varies across different months. R^2
412 in winter months are 0.76, 0.36 and 0.61, in November, December and February, respectively, while R^2 exceeds 0.9 in
413 other months. This unexpectedly low R^2 only occurs in the winter months at the overlapping size range. It can be



414 speculated that the measurements by the two instruments differ in a larger extent during winter. This might be attributed
415 to sensor drift and a number of interference artefacts for particle measurements associated with several factors, such as
416 relative humidity, temperature and other gas-phase species, which were demonstrated by several researchers (Lewis et
417 al., 2016; Popoola et al., 2016). Another reason for the difference in model performance can be that the percentage of
418 complete rows in these months are lower than the other months. The drop in data points might impose an influence to the
419 modelling performance. Especially in June, at the few size bins close to the larger edge, R^2 ranges from 0.9 to 0.7. Besides
420 that, some low R^2 can be also found in individual month at both edges of size range, which does not appear to show any
421 patterns.

422

423 In short, the prediction ability for lower edge ($0.01 < D_p < 0.03 \mu\text{m}$) is found worse in both models. The model performance
424 in mid-range ($0.15 < D_p < 0.5 \mu\text{m}$) and upper edge ($6 < D_p < 10 \mu\text{m}$) are relatively worse for model with other fractionated
425 size bins as input variables according to the aforementioned statistical performance indicators. All statistical prediction
426 simulations are based on the previous history of relationships between the inputs and outputs. As a result, the prediction
427 simulations for different size ranges have significantly unique connections. The model by meteorological parameters
428 considers only 6 predictor variables so the accuracy is lower than the model by PSD. It might not seem surprising that the
429 deviations between the measured and estimated size distribution were not substantial ($R^2 > 0.97$, $\text{NRMSE} < 0.25$) because
430 the PSD model take 22 other size bins as predictor variables. This, still, gives a clue that the proposed model can provide
431 adequate solutions to particle size distribution prognostic demands. The estimation of certain bin size by other bin sizes
432 can be thought of replacing ‘negative’ values in the raw data by particle sizers, including SMPS we used in this paper.
433 Instead of eliminating the negative values, they can be estimated by other size bins with a high accuracy in order to keep
434 the symmetry in data error distribution (Viskari et al., 2012).

435 5 Conclusion

436 This paper presents the evaluation of feed-forward neural network (FFNN) models for estimating particle number
437 concentration at various particulate size bins. Input predictors include a merged particle size distribution, by a scanning
438 mobility particle sizer (NanoSMPS) and an optical particle sizer (OPS), which covers size range from 0.01 to 10, and
439 meteorological parameters, including temperature (Temp), relative humidity (RH), wind speed (WS), wind direction
440 (WD) and ambient pressure (P). The measurements were collected in an urban background region in Amman, the capital
441 of Jordan in the period of 1st Aug 2016–31st July 2017. The total number concentration ($1.70 \pm 1.26 \times 10^4 \text{ cm}^{-3}$) in the
442 measurement period show moderate seasonal variability owing to the more suppressed boundary layer (Teinilä et al.,
443 2019) and the elevated wood combustion (Hellén et al., 2017) in wintertime. Similar to many other urban environments,
444 the diurnal pattern observed in this study reflects the traffic activity, which has a more pronounced pattern during
445 workdays (Hussein et al., 2019). The amount of coarse particles is trivial in terms of number concentration but dust
446 episodes were found often in spring during the measurement period.

447

448 We proposed three approaches with different input variables: (1) only meteorological parameters, (2) only number
449 concentration at the remaining size bins, and (3) both of the above. We performed optimisation to obtain the optimal
450 configuration of the FFNN models, which are two layers with 10–15 neurons, balancing the accuracy and the computing
451 resources. The 5-min averaged meteorological parameters give varying number concentration estimation for various size
452 bins ($R^2 = 0.22\text{--}0.58$), which is outperformed by hourly and daily averaged data ($R^2 = 0.66\text{--}0.77$), as demonstrated by



453 (Zaidan et al., 2020). The models using the number concentration at the remaining size bins, both with or without
454 meteorological data, show expected perfect performance ($R^2 > 0.97$).

455

456 Relatively poor model performance is found in three regions. At the lower edge ($0.01 < D_p < 0.02 \mu\text{m}$) and the upper edge
457 ($6 < D_p < 10 \mu\text{m}$), the number of neighbouring size bins is limited and also the detection efficiency by the corresponding
458 instruments is lower compared to the other size bins. Another noticeable region ($0.15 < D_p < 0.5 \mu\text{m}$) is the overlapping
459 section measured by the two particle sizers and the reason is because of the deficiency of merging algorithm. For all the
460 above approaches, the poorer performance for smaller particles in the nucleation mode could be due to the fact that it is
461 more effectively removed from the atmosphere compared to other modes (Al-Dabbous et al., 2017). An observable
462 overestimation is also found in early morning for ultrafine particles followed by a distinct underestimation before midday.
463 A larger derivation between the measured and the estimated number concentration is found in the winter, which might be
464 caused by sensor drift and interference artefacts (Lewis et al., 2016; Popoola et al., 2016). Despite the high number of
465 input predictors, the good model performance provides an alternative method to fill up the negative values in size
466 distribution raw dataset, which often exist due to ill-configured problems. Instead of removing the factually impossible
467 data point, this way of replacing negative numbers can maintain a symmetric distribution of errors (Viskari et al., 2012)
468 and minimise the uncertainties caused.

469 **Code/Data availability**

470 The code and data is available upon request.

471 **Author contribution**

472 TH and MZ designed the experiments and TH carried them out. PLF and OS developed the model code. PLF prepared
473 the manuscript with contributions from all co-authors.

474 **Competing interests**

475 The authors declare that they have no conflict of interest.

476 **References**

- 477 Ahmed, R., Robinson, R., and Mortimer, K.: The epidemiology of noncommunicable respiratory disease in sub-Saharan
478 Africa, the Middle East, and North Africa, *Malawi Med J*, 29, 203-211, 10.4314/mmj.v29i2.24, 2017.
- 479 Al-Dabbous, A. N., Kumar, P., and Khan, A. R.: Prediction of airborne nanoparticles at roadside location using a feed-
480 forward artificial neural network, *Atmos Pollut Res*, 8, 446-454, 10.1016/j.apr.2016.11.004, 2017.
- 481 Arhami, M., Shahne, M. Z., Hosseini, V., Haghghat, N. R., Lai, A. M., and Schauer, J. J.: Seasonal trends in the
482 composition and sources of PM_{2.5} and carbonaceous aerosol in Tehran, Iran, *Environ Pollut*, 239, 69-81,
483 10.1016/j.envpol.2018.03.111, 2018.
- 484 Borgie, M., Ledoux, F., Dagher, Z., Verdin, A., Cazier, F., Courcot, L., Shirali, P., Greige-Gerges, H., and Courcot, D.:
485 Chemical characteristics of PM_{2.5-0.3} and PM_{0.3} and consequence of a dust storm episode at an urban site in Lebanon,
486 *Atmospheric Research*, 180, 274-286, 10.1016/j.atmosres.2016.06.001, 2016.
- 487 Cabaneros, S. M., Calautit, J. K., and Hughes, B. R.: A review of artificial neural network models for ambient air pollution
488 prediction, *Environmental Modelling & Software*, 119, 285-304, 10.1016/j.envsoft.2019.06.014, 2019.



- 489 Cai, R., Yang, D., Ahonen, L. R., Shi, L., Korhonen, F., Ma, Y., Hao, J., Petäjä, T., Zheng, J., Kangasluoma, J., and Jiang,
490 J.: Data inversion methods to determine sub-3 nm aerosol size distributions using the particle size magnifier, *Atmos.*
491 *Meas. Tech.*, 11, 4477-4491, 10.5194/amt-11-4477-2018, 2018.
- 492 Chaloulakou, A., Grivas, G., and Spyrellis, N.: Neural network and multiple regression models for PM10 prediction in
493 Athens: a comparative assessment, *J Air Waste Manag Assoc*, 53, 1183-1190, 10.1080/10473289.2003.10466276, 2003.
- 494 Clifford, S., Low Choy, S., Hussein, T., Mengersen, K., and Morawska, L.: Using the Generalised Additive Model to
495 model the particle number count of ultrafine particles, *Atmospheric Environment*, 45, 5934-5945,
496 10.1016/j.atmosenv.2011.05.004, 2011.
- 497 DeCarlo, P. F., Slowik, J. G., Worsnop, D. R., Davidovits, P., and Jimenez, J. L.: Particle morphology and density
498 characterization by combined mobility and aerodynamic diameter measurements. Part 1: Theory, *Aerosol Sci Tech*, 38,
499 1185-1205, 10.1080/027868290903907, 2004.
- 500 Enting, I., and Newsam, G.: Atmospheric constituent inversion problems: Implications for baseline monitoring, *Journal*
501 *of Atmospheric Chemistry*, 11, 69-87, 1990.
- 502 Fonseca, A. S., Viana, M., Perez, N., Alastuey, A., Querol, X., Kaminski, H., Todea, A. M., Monz, C., and Asbach, C.:
503 Intercomparison of a portable and two stationary mobility particle sizers for nanoscale aerosol measurements, *Aerosol*
504 *Sci Tech*, 50, 653-668, 10.1080/02786826.2016.1174329, 2016.
- 505 Freeman, B. S., Taylor, G., Gharabaghi, B., and Thé, J.: Forecasting air quality time series using deep learning, *Journal*
506 *of the Air & Waste Management Association*, 68, 866-886, 10.1080/10962247.2018.1459956, 2018.
- 507 Fung, P. L., Zaidan, M. A., Timonen, H., Niemi, J. V., Kousa, A., Kuula, J., Luoma, K., Tarkoma, S., Petäjä, T., Kulmala,
508 M., and Hussein, T.: Evaluation of white-box versus black-box machine learning models in estimating ambient black
509 carbon concentration, *Journal of Aerosol Science*, 10.1016/j.jaerosci.2020.105694, 2020.
- 510 Gerling, L., Loschau, G., Wiedensohler, A., and Weber, S.: Statistical modelling of roadside and urban background
511 ultrafine and accumulation mode particle number concentrations using generalized additive models, *Sci Total Environ*,
512 703, 134570, 10.1016/j.scitotenv.2019.134570, 2020.
- 513 Gherboudj, I., Beegum, S. N., and Ghedira, H.: Identifying natural dust source regions over the Middle-East and North-
514 Africa: Estimation of dust emission potential, *Earth-Sci Rev*, 165, 342-355, 10.1016/j.earscirev.2016.12.010, 2017.
- 515 Goudarzi, G., Shirmardi, M., Naimabadi, A., Ghadiri, A., and Sajedifar, J.: Chemical and organic characteristics of PM2.5
516 particles and their in-vitro cytotoxic effects on lung cells: The Middle East dust storms in Ahvaz, Iran, *Sci Total Environ*,
517 655, 434-445, 10.1016/j.scitotenv.2018.11.153, 2019.
- 518 Gupta, R., and Xie, H.: Nanoparticles in Daily Life: Applications, Toxicity and Regulations, *J Environ Pathol Toxicol*
519 *Oncol*, 37, 209-230, 10.1615/JEnvironPatholToxicolOncol.2018026009, 2018.
- 520 Hakala, S., Alghamdi, M. A., Paasonen, P., Vakkari, V., Khoder, M. I., Neitola, K., Dada, L., Abdelmaksoud, A. S., Al-
521 Jeelani, H., Shabbaj, I. I., Almeahadi, F. M., Sundström, A. M., Lihavainen, H., Kerminen, V. M., Kontkanen, J.,
522 Kulmala, M., Hussein, T., and Hyvärinen, A. P.: New particle formation, growth and apparent shrinkage at a rural
523 background site in western Saudi Arabia, *Atmos. Chem. Phys.*, 19, 10537-10555, 10.5194/acp-19-10537-2019, 2019.
- 524 Hellén, H., Kangas, L., Kousa, A., Vestenius, M., Teinilä, K., Karppinen, A., Kukkonen, J., and Niemi, J. V.: Evaluation
525 of the impact of wood combustion on benzo[a]pyrene (BaP) concentrations; ambient measurements and dispersion
526 modeling in Helsinki, Finland, *Atmospheric Chemistry and Physics*, 17, 3475-3487, 10.5194/acp-17-3475-2017, 2017.
- 527 Hussein, T., Dal Maso, M., Petäjä, T., Koponen, I. K., Paatero, P., Aalto, P. P., Hämeri, K., and Kulmala, M.: Evaluation
528 of an automatic algorithm for fitting the particle number size distributions, *Boreal Environment Research*, 10, 337-355,
529 2005.
- 530 Hussein, T., Kukkonen, J., Korhonen, H., Pohjola, M., Pirjola, L., Wraith, D., Harkonen, J., Teinila, K., Koponen, I. K.,
531 Karppinen, A., Hillamo, R., and Kulmala, M.: Evaluation and modeling of the size fractionated aerosol particle number
532 concentration measurements nearby a major road in Helsinki – Part II: Aerosol measurements within the SAPHIRE
533 project, *Atmospheric Chemistry and Physics*, 7, 4081-4094, 10.5194/acp-7-4081-2007, 2007.
- 534 Hussein, T., Dada, L., Hakala, S., Petäjä, T., and Kulmala, M.: Urban Aerosol Particle Size Characterization in Eastern
535 Mediterranean Conditions, *Atmosphere*, 10, 10.3390/atmos10110710, 2019.
- 536 Hussein, T., Atashi, N., Sogacheva, L., Hakala, S., Dada, L., Petäjä, T., and Kulmala, M.: Characterization of Urban New
537 Particle Formation in Amman—Jordan, *Atmosphere*, 11, 10.3390/atmos11010079, 2020.
- 538 Kandlikar, M., and Ramachandran, G.: Inverse methods for analysing aerosol spectrometer measurements: a critical
539 review, *Journal of Aerosol Science*, 30, 413-437, 1999.
- 540 Kannosto, J., Virtanen, A., Lemmetty, M., Mäkelä, J. M., Keskinen, J., Junninen, H., Hussein, T., Aalto, P., and Kulmala,
541 M.: Mode resolved density of atmospheric aerosol particles, *Atmos. Chem. Phys.*, 8, 5327-5337, 10.5194/acp-8-5327-
542 2008, 2008.
- 543 Kerminen, V. M., Paramonov, M., Anttila, T., Riipinen, I., Fountoukis, C., Korhonen, H., Asmi, E., Laakso, L.,
544 Lihavainen, H., Swietlicki, E., Svenningsson, B., Asmi, A., Pandis, S. N., Kulmala, M., and Petaja, T.: Cloud
545 condensation nuclei production associated with atmospheric nucleation: a synthesis based on existing literature and new
546 results, *Atmospheric Chemistry and Physics*, 12, 12037-12059, 10.5194/acp-12-12037-2012, 2012.
- 547 Kerminen, V. M., Chen, X. M., Vakkari, V., Petaja, T., Kulmala, M., and Bianchi, F.: Atmospheric new particle formation
548 and growth: review of field observations, *Environ Res Lett*, 13, 10.1088/1748-9326/aadf3c, 2018.



- 549 Kok, J. F., Ridley, D. A., Zhou, Q., Miller, R. L., Zhao, C., Heald, C. L., Ward, D. S., Albani, S., and Haustein, K.:
550 Smaller desert dust cooling effect estimated from analysis of dust size and abundance, *Nat Geosci*, 10, 274-278,
551 10.1038/Ngeo2912, 2017.
- 552 Kreyling, W. G., Semmler, M., and Moller, W.: Dosimetry and toxicology of ultrafine particles, *J Aerosol Med*, 17, 140-
553 152, 10.1089/0894268041457147, 2004.
- 554 Kulkarni, P., Baron, P. A., and Willeke, K.: *Aerosol measurement: principles, techniques, and applications*, John Wiley
555 & Sons, 2011.
- 556 Kulmala, M., Vehkamäki, H., Petaja, T., Dal Maso, M., Lauri, A., Kerminen, V. M., Birmili, W., and McMurry, P. H.:
557 Formation and growth rates of ultrafine atmospheric particles: a review of observations, *Journal of Aerosol Science*, 35,
558 143-176, 10.1016/j.jaerosci.2003.10.003, 2004.
- 559 Laakso, L., Hussein, T., Aarnio, P., Komppula, M., Hiltunen, V., Viisanen, Y., and Kulmala, M.: Diurnal and annual
560 characteristics of particle mass and number concentrations in urban, rural and Arctic environments in Finland,
561 *Atmospheric Environment*, 37, 2629-2641, 10.1016/S1352-2310(03)00206-1, 2003.
- 562 Lehtipalo, K., Leppä, J., Kontkanen, J., Kangasluoma, J., Franchin, A., Wimmer, D., Schobesberger, S., Junninen, H.,
563 Petaja, T., and Sipilä, M. J. B. E. R.: Methods for determining particle size distribution and growth rates between 1 and 3
564 nm using the Particle Size Magnifier, 2014.
- 565 Lelieveld, J., Evans, J. S., Fnais, M., Giannadaki, D., and Pozzer, A.: The contribution of outdoor air pollution sources to
566 premature mortality on a global scale, *Nature*, 525, 367-371, 10.1038/nature15371, 2015.
- 567 Lewis, A. C., Lee, J. D., Edwards, P. M., Shaw, M. D., Evans, M. J., Moller, S. J., Smith, K. R., Buckley, J. W., Ellis,
568 M., Gillot, S. R., and White, A.: Evaluating the performance of low cost chemical sensors for air pollution research,
569 *Faraday Discuss*, 189, 85-103, 10.1039/c5fd00201j, 2016.
- 570 Liu, Z. R., Hu, B., Liu, Q., Sun, Y., and Wang, Y. S.: Source apportionment of urban fine particle number concentration
571 during summertime in Beijing, *Atmospheric Environment*, 96, 359-369, 10.1016/j.atmosenv.2014.06.055, 2014.
- 572 Londahl, J., Moller, W., Pagels, J. H., Kreyling, W. G., Swietlicki, E., and Schmid, O.: Measurement techniques for
573 respiratory tract deposition of airborne nanoparticles: a critical review, *J Aerosol Med Pulm Drug Deliv*, 27, 229-254,
574 10.1089/jamp.2013.1044, 2014.
- 575 Maleki, H., Sorooshian, A., Goudarzi, G., Baboli, Z., Birgani, Y. T., and Rahmati, M.: Air pollution prediction by using
576 an artificial neural network model, *Clean Technologies and Environmental Policy*, 21, 1341-1352, 10.1007/s10098-019-
577 01709-w, 2019.
- 578 Markowski, G. R.: Improving Twomey's algorithm for inversion of aerosol measurement data, *Aerosol Sci Tech*, 7, 127-
579 141, 1987.
- 580 Mølgaard, B., Birmili, W., Clifford, S., Massling, A., Eleftheriadis, K., Norman, M., Vratolis, S., Wehner, B., Corander,
581 J., Hämeri, K., and Hussein, T.: Evaluation of a statistical forecast model for size-fractionated urban particle number
582 concentrations using data from five European cities, *Journal of Aerosol Science*, 66, 96-110,
583 10.1016/j.jaerosci.2013.08.012, 2013.
- 584 Morawska, L., Ristovski, Z., Jayaratne, E. R., Keogh, D. U., and Ling, X.: Ambient nano and ultrafine particles from
585 motor vehicle emissions: Characteristics, ambient processing and implications on human exposure, *Atmospheric*
586 *Environment*, 42, 8113-8138, 10.1016/j.atmosenv.2008.07.050, 2008.
- 587 Ohlwein, S., Kappeler, R., Joss, M. K., Kunzli, N., and Hoffmann, B.: Health effects of ultrafine particles: a systematic
588 literature review update of epidemiological evidence, *Int J Public Health*, 64, 547-559, 10.1007/s00038-019-01202-7,
589 2019.
- 590 Popoola, O. A. M., Stewart, G. B., Mead, M. I., and Jones, R. L.: Development of a baseline-temperature correction
591 methodology for electrochemical sensors and its implications for long-term stability, *Atmospheric Environment*, 147,
592 330-343, 10.1016/j.atmosenv.2016.10.024, 2016.
- 593 Rahman, M. M., Mazaheri, M., Clifford, S., and Morawska, L.: Estimate of main local sources to ambient ultrafine particle
594 number concentrations in an urban area, *Atmospheric Research*, 194, 178-189, 10.1016/j.atmosres.2017.04.036, 2017.
- 595 Reggente, M., Peters, J., Theunis, J., Van Poppel, M., Rademaker, M., Kumar, P., and De Baets, B.: Prediction of ultrafine
596 particle number concentrations in urban environments by means of Gaussian process regression based on measurements
597 of oxides of nitrogen, *Environmental Modelling & Software*, 61, 135-150, 10.1016/j.envsoft.2014.07.012, 2014.
- 598 Rönkkö, T., Kuuluvainen, H., Karjalainen, P., Keskinen, J., Hillamo, R., Niemi, J. V., Pirjola, L., Timonen, H. J.,
599 Saarikoski, S., Saukko, E., Jarvinen, A., Silvennoinen, H., Rostedt, A., Olin, M., Yli-Ojanpera, J., Nousiainen, P., Kousa,
600 A., and Dal Maso, M.: Traffic is a major source of atmospheric nanocluster aerosol, *P Natl Acad Sci USA*, 114, 7549-
601 7554, 10.1073/pnas.1700830114, 2017.
- 602 Rudin, C.: Stop explaining black box machine learning models for high stakes decisions and use interpretable models
603 instead, *Nature machine intelligence*, 1, 206-215, 10.1038/s42256-019-0048-x, 2019.
- 604 Sabaliauskas, K., Jeong, C. H., Yao, X. H., Jun, Y. S., Jadidian, P., and Evans, G. J.: Five-year roadside measurements
605 of ultrafine particles in a major Canadian city, *Atmospheric Environment*, 49, 245-256, 10.1016/j.atmosenv.2011.11.052,
606 2012.



607 Spinazzè, A., Fanti, G., Borghi, F., Del Buono, L., Campagnolo, D., Rovelli, S., Cattaneo, A., and Cavallo, D. M.: Field
608 comparison of instruments for exposure assessment of airborne ultrafine particles and particulate matter, *Atmospheric*
609 *Environment*, 154, 274–284, 10.1016/j.atmosenv.2017.01.054, 2017.

610 Stolzenburg, M. R., and McMurry, P. H.: Method to assess performance of scanning mobility particle sizer (SMPS)
611 instruments and software, *Aerosol Sci Tech*, 52, 609–613, 10.1080/02786826.2018.1455962, 2018.

612 Teinilä, K., Aurela, M., Niemi, J. V., Kousa, A., Petäjä, T., Järvi, L., Hillamo, R., Kangas, L., Saarikoski, S., and Timonen,
613 H.: Concentration variation of gaseous and particulate pollutants in the Helsinki city centre — observations from a two-
614 year campaign from 2013–2015, *Boreal Environment Research*, 24, 115–136, 2019.

615 Tritscher, T., Beeston, M., Zerrath, A. F., Elzey, S., Krinke, T. J., Filimundi, E., and Bischof, O. F.: NanoScan SMPS -
616 A Novel, Portable Nanoparticle Sizing and Counting Instrument, *J Phys Conf Ser*, 429, 10.1088/1742-
617 6596/429/1/012061, 2013.

618 Tritscher, T., Koched, A., Han, H. S., Filimundi, E., Johnson, T., Elzey, S., Avenido, A., Kykal, C., and Bischof, O. F.:
619 Multi-Instrument Manager Tool for Data Acquisition and Merging of Optical and Electrical Mobility Size Distributions,
620 4th International Conference on Safe Production and Use of Nanomaterials (Nanosafe2014), 617, 10.1088/1742-
621 6596/617/1/012013, 2015.

622 Viskari, T., Asmi, E., Kolmonen, P., Vuollekoski, H., Petaja, T., and Jarvinen, H.: Estimation of aerosol particle number
623 distributions with Kalman Filtering - Part 1: Theory, general aspects and statistical validity, *Atmospheric Chemistry and*
624 *Physics*, 12, 11767–11779, 10.5194/acp-12-11767-2012, 2012.

625 Wiedensohler, A., Birmili, W., Nowak, A., Sonntag, A., Weinhold, K., Merkel, M., Wehner, B., Tuch, T., Pfeifer, S.,
626 Fiebig, M., Fjåraa, A. M., Asmi, E., Sellegri, K., Depuy, R., Venzac, H., Villani, P., Laj, P., Aalto, P., Ogren, J. A.,
627 Swietlicki, E., Williams, P., Roldin, P., Quincey, P., Hüglin, C., Fierz-Schmidhauser, R., Gysel, M., Weingartner, E.,
628 Riccobono, F., Santos, S., Gruning, C., Faloon, K., Beddows, D., Harrison, R., Monahan, C., Jennings, S. G., O'Dowd,
629 C. D., Marinoni, A., Horn, H. G., Keck, L., Jiang, J., Scheckman, J., McMurry, P. H., Deng, Z., Zhao, C. S., Moerman,
630 M., Henzing, B., de Leeuw, G., Löschau, G., and Bastian, S.: Mobility particle size spectrometers: harmonization of
631 technical standards and data structure to facilitate high quality long-term observations of atmospheric particle number
632 size distributions, *Atmos. Meas. Tech.*, 5, 657–685, 10.5194/amt-5-657-2012, 2012.

633 Population growth (annual %): <https://data.worldbank.org/indicator/SP.POP.GROW>, access: 06-10, 2019.

634 World Health Organisation: World health statistics 2019: Monitoring health for the SDGs, sustainable development goals,
635 World Health Organisation, <https://apps.who.int/iris/handle/10665/324835>, 2019.

636 Xing, Y. F., Xu, Y. H., Shi, M. H., and Lian, Y. X.: The impact of PM_{2.5} on the human respiratory system, *J Thorac Dis*,
637 8, E69–74, 10.3978/j.issn.2072-1439.2016.01.19, 2016.

638 Zaidan, M. A., Canova, F. F., Laurson, L., and Foster, A. S.: Mixture of Clustered Bayesian Neural Networks for
639 Modeling Friction Processes at the Nanoscale, *J Chem Theory Comput*, 13, 3–8, 10.1021/acs.jctc.6b00830, 2017.

640 Zaidan, M. A., Wraith, D., Boor, B. E., and Hussein, T.: Bayesian Proxy Modelling for Estimating Black Carbon
641 Concentrations using White-Box and Black-Box Models, *Applied Sciences*, 9, 10.3390/app9224976, 2019.

642 Zaidan, M. A., Surakhi, O., Fung, P. L., and Hussein, T.: Sensitivity Analysis for Predicting Sub-Micron Aerosol
643 Concentrations Based on Meteorological Parameters, *Sensors (Basel)*, 20, 10.3390/s20102876, 2020.

644 Zhou, Y., Dada, L., Liu, Y., Fu, Y., Kangasluoma, J., Chan, T., Yan, C., Chu, B., Daellenbach, K. R., Bianchi, F. J. A.
645 C., and Physics: Variation of size-segregated particle number concentrations in wintertime Beijing, 20, 1201–1216, 2020.

646

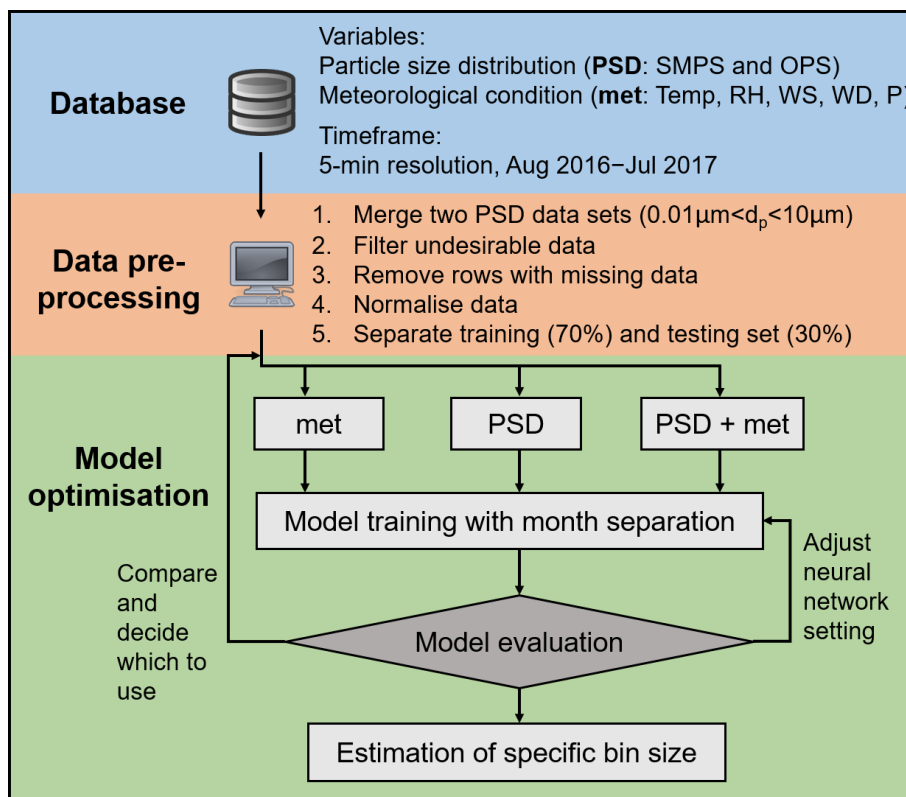


Figure 1. The block diagram describing the methodology of the model.

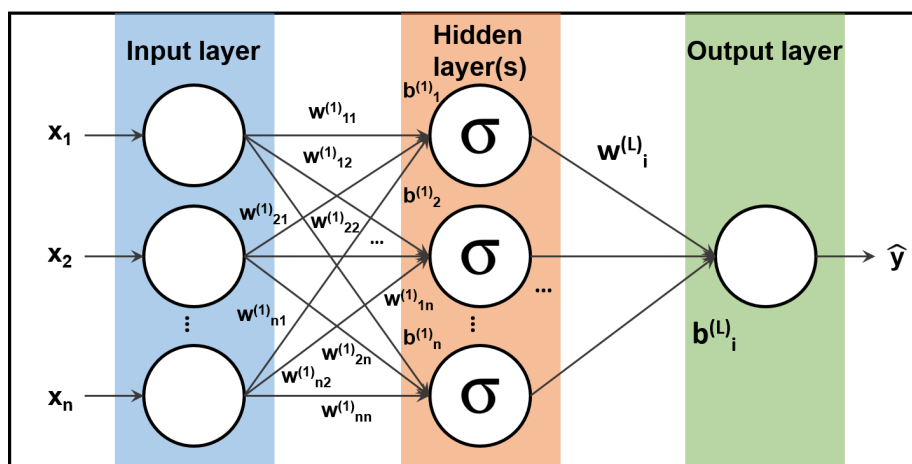


Figure 2. Schematic diagram of a neural network with one hidden layer of sigmoid activation function.

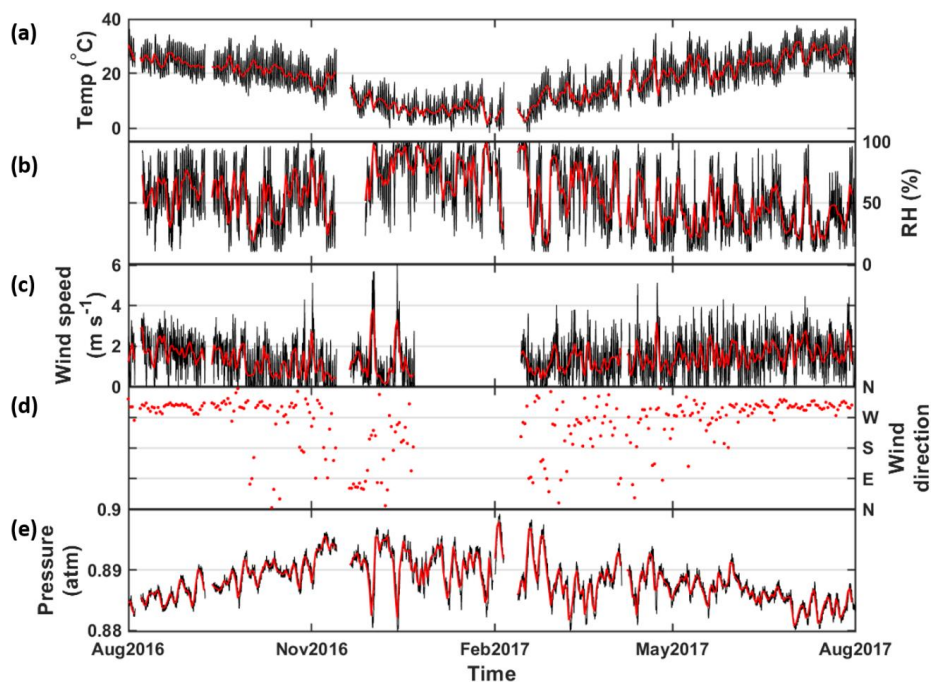


Figure 3. Timeseries of meteorological conditions during the measurement period Aug 2016–Jul 2017. (a–e) denotes temperature, relative humidity, wind speed, wind direction and air pressure, respectively. Black and red represent hourly and daily averaged data, respectively.

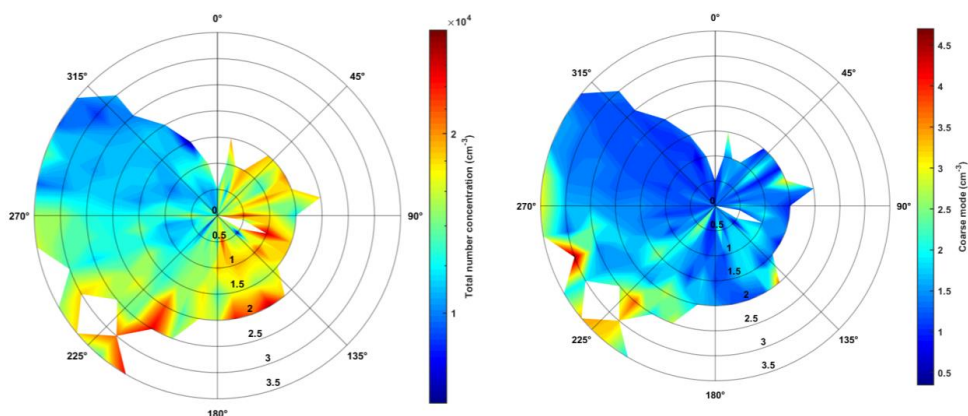


Figure 4. Windrose diagram of total particle number concentration at different direction (in theta axis) and different wind speed (in radial axis). Wind direction and wind speed data are grouped in every 10° and 0.5 m s^{-1} . Warmer color represent higher total particle number concentration. (a) total number concentration, log scale; (b) coarse mode, linear scale. Note the color scales are different.

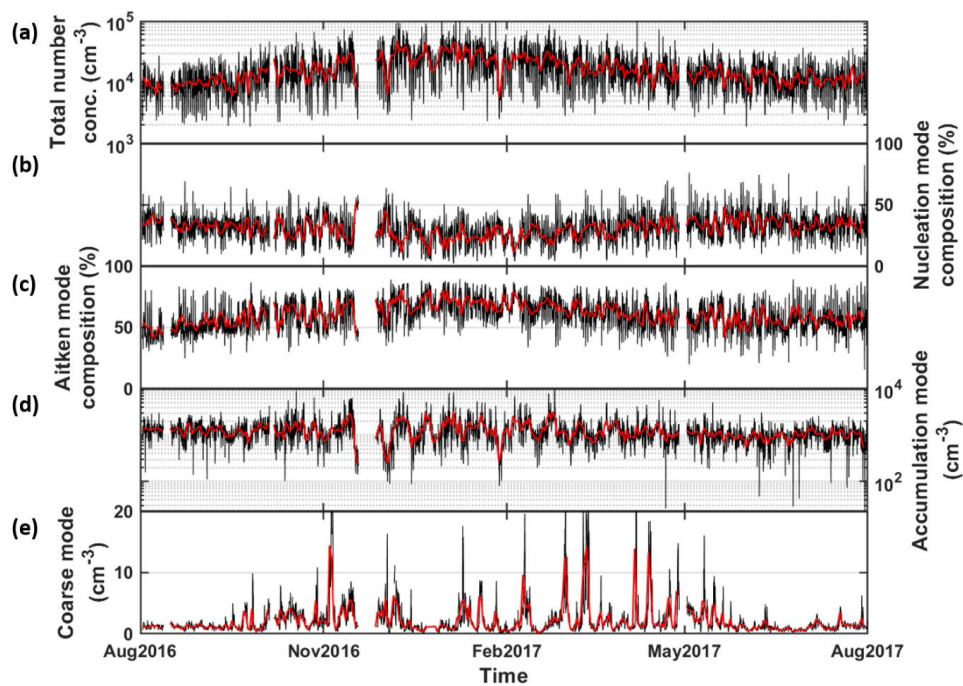


Figure 5. Timeseries of total particle number concentration (in cm^{-3}) of $0.01\text{--}10\mu\text{m}$ in (a). (b–c) indicate the composition in percentage of nucleation mode and Aitken mode, respectively. (d–e) show the number concentration in accumulation mode and coarse mode, respectively. Black and red represent hourly and daily averaged data, respectively.

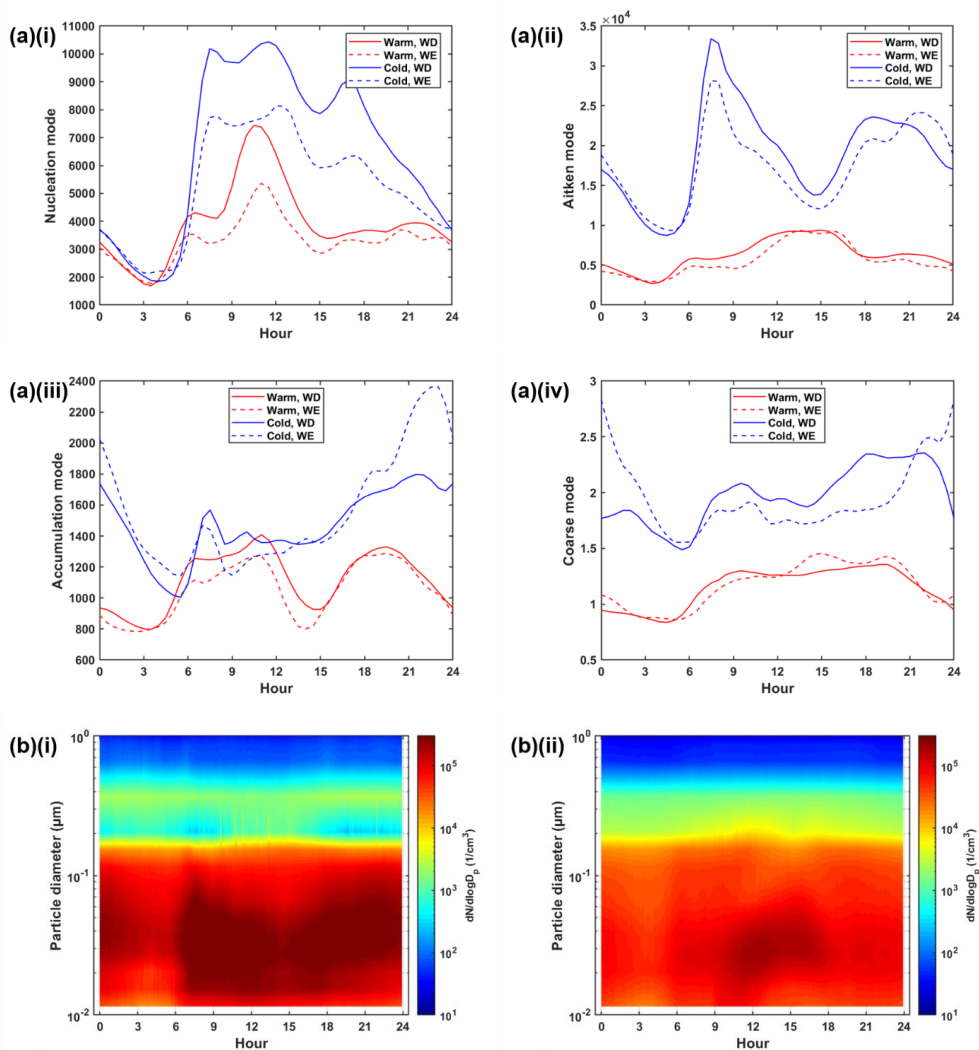


Figure 6. (a) Diurnal cycle of the (i) nucleation mode, (ii) Aitken mode, (iii) accumulation mode and (iv) coarse mode in warm (red) and cold months (blue) during workdays (solid) and weekends (dashed). (b) Particle size distribution in (i) cold and (ii) warm months, coloured by particle number concentration (cm^{-3}).

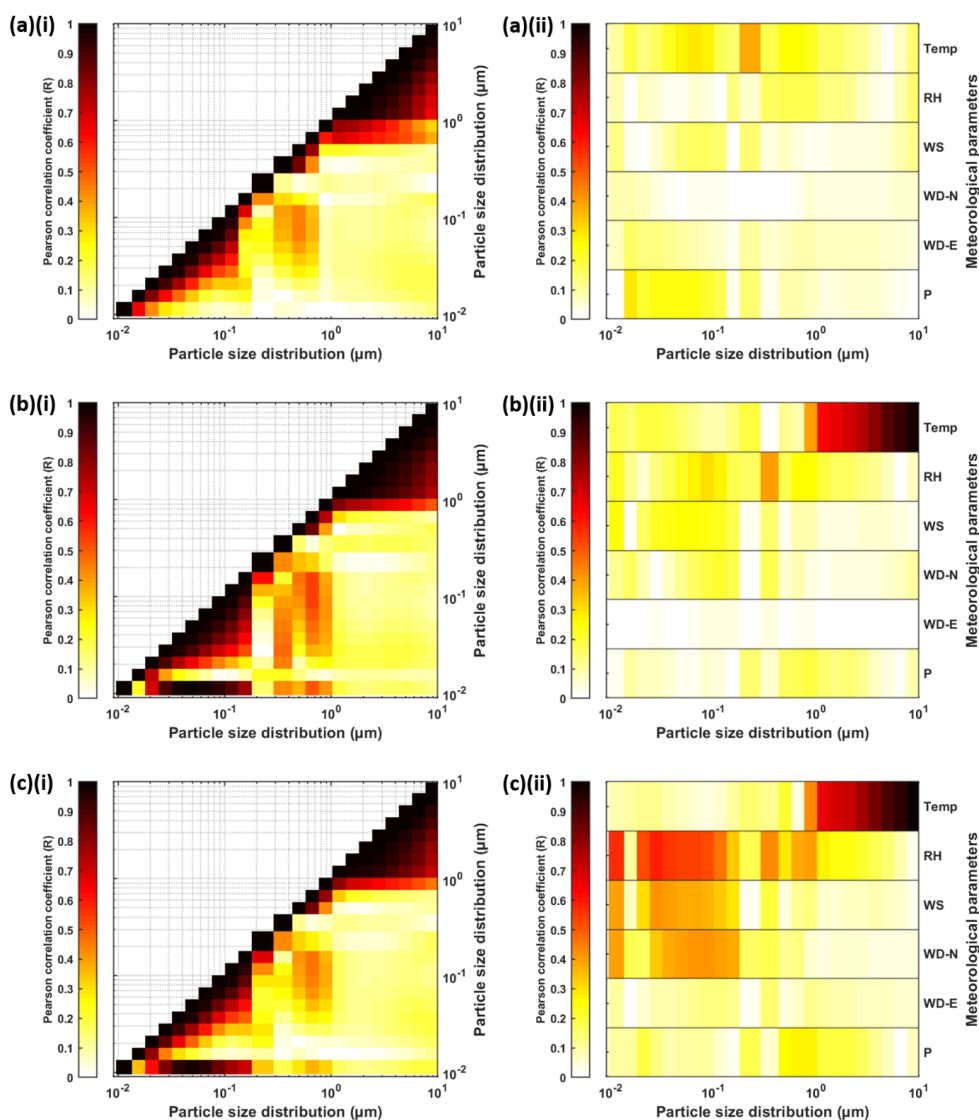
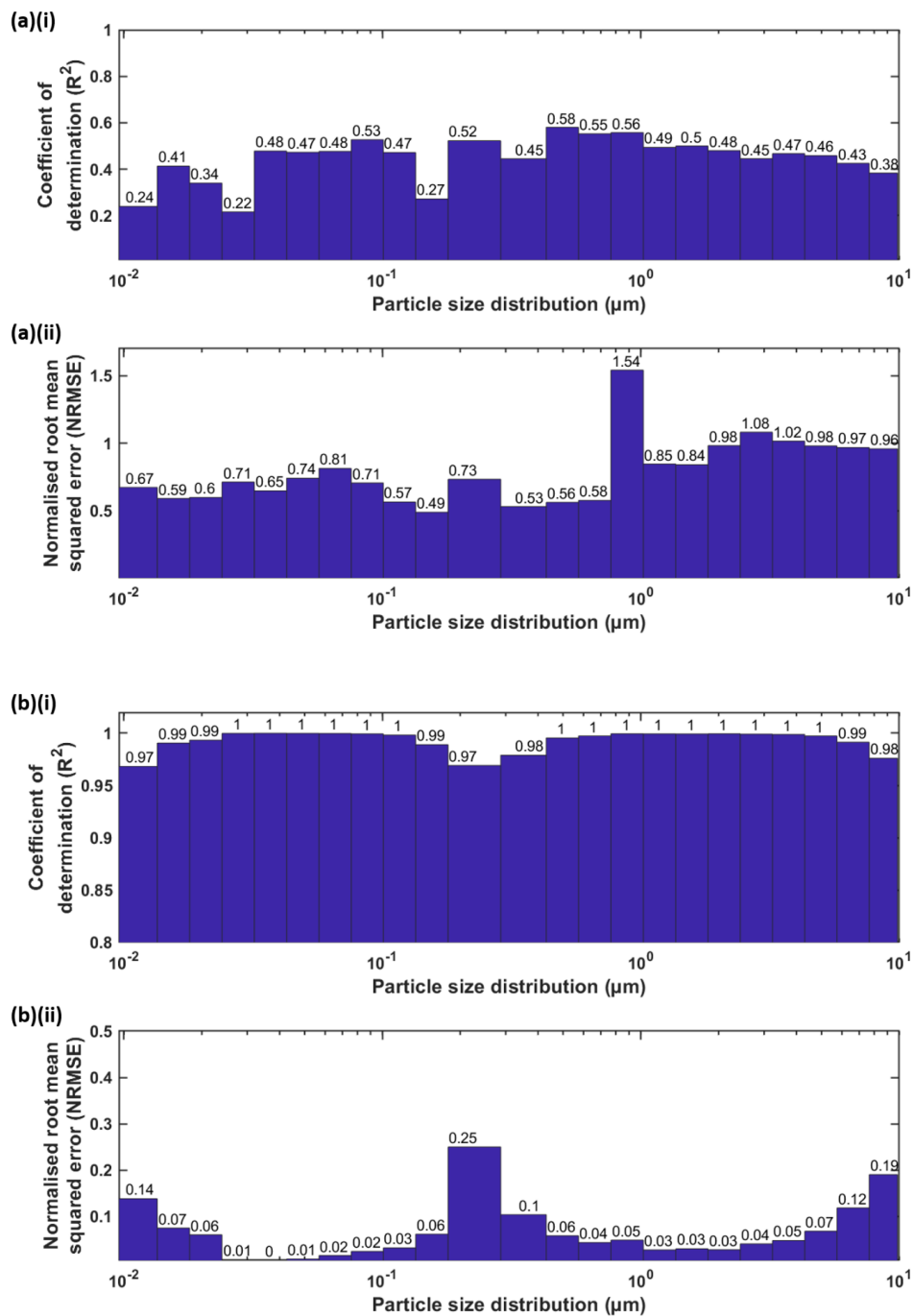


Figure 7. Matrix plots showing the Pearson correlation coefficient (R) of particle size distribution of (a) 5-min, (b) hourly, (c) daily averaging with (i) particle size distribution itself and (ii) meteorological parameters. Darker colour represents a higher correlation.



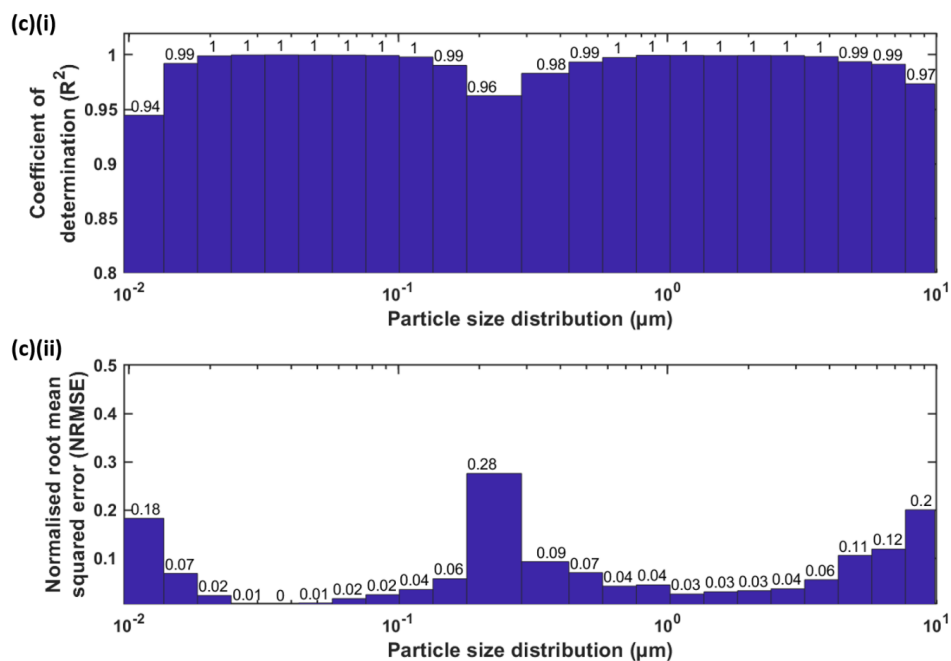


Figure 8. Bar chart showing the model evaluation of model with (a) only meteorological parameters, (b) particle size distribution itself, (c) both particle size distribution and meteorological parameters as inputs. The model evaluation metrics include (i) coefficient of determination (R^2) and (ii) normalised root mean squared error (NRMSE).

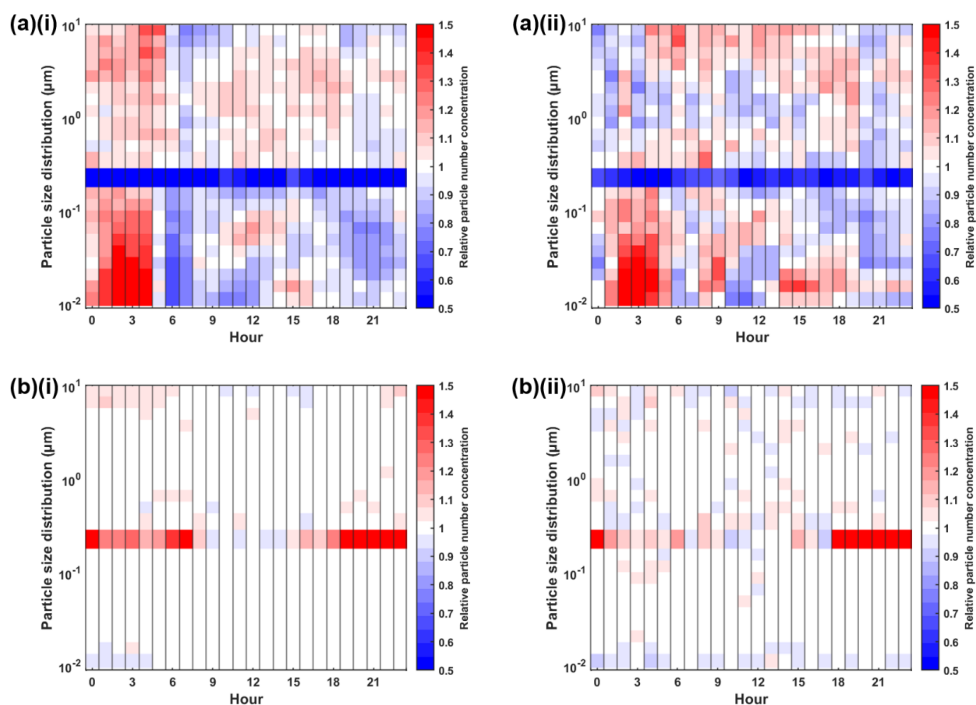


Figure 9. Heatmap showing the hourly median relative particle number concentration of the models with (a) meteorological parameters and (b) particle size distribution as input across different hours of a day (i) in workdays and (ii) in weekends. The relative particle number concentration is defined as modelled concentration with respect to measured concentration. Red colour show overestimation while blue show underestimation.

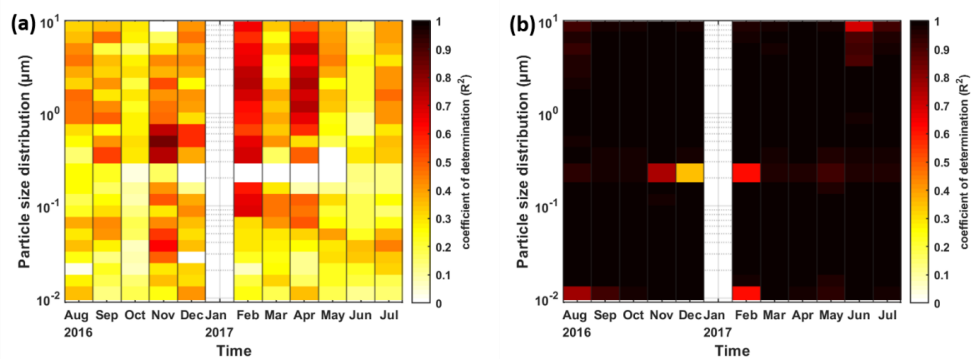


Figure 10. Heatmap showing the coefficient of determination (R^2) of the models with (a) meteorological parameters and (b) particle size distribution as input for different months at different size bins. Darker colour represents a higher R^2 .



656 Table 1. Table showing the descriptive statistics (in cm^{-3}) of total number concentration, nucleation mode, Aitken mode,
 657 accumulation mode and coarse mode. The statistical values include mean, standard deviation, and percentile (10%, 25%,
 658 50%, 75% and 90%).

	Mean	std	10%	25%	50%	75%	90%
Total ($\times 10^4$)	1.70	1.26	0.57	0.85	1.35	2.16	3.31
Nucleation ($\times 10^4$)	0.48	0.32	0.16	0.26	0.41	0.63	0.90
Aitken ($\times 10^4$)	1.09	1.01	0.29	0.45	0.77	1.37	2.35
Accumulation ($\times 10^4$)	0.13	0.08	0.05	0.08	0.11	0.15	0.21
Coarse	2.13	2.80	0.55	0.84	1.29	2.33	4.3

659

660 Table 2. Table showing the best configuration in the form of (the number of layers; the number of neurons) for the model
 661 by meteorological parameters and the number concentration at the other size bins. Mean absolute error (MAE, in cm^{-3}),
 662 coefficient of determination (R^2) and normalised root-mean-square error (NRMSE) are listed for different size bins on
 663 each row. The last row concludes the overall selection of the model with the best configuration and its corresponding
 664 evaluation metrics.

Particle size (μm)	Approach 1 (met)				Approach 2 (PSD)			
	Best setting	MAE (cm^{-3})	R^2	NRMSE	Best setting	MAE (cm^{-3})	R^2	NRMSE
0.012	2; 10	2638.6	0.1996	0.6918	2; 10	333.7442	0.99	0.1077
0.015	2; 15	4853.0	0.4237	0.5868	2; 8	215.8006	1.00	0.0310
0.021	2; 15	6119.1	0.3774	0.5831	2; 15	97.8408	1.00	0.0136
0.027	2; 15	8469.2	0.4072	0.6210	1; 25	34.0126	1.00	0.0032
0.037	2; 20	8235.7	0.4568	0.6619	2; 15	26.2854	1.00	0.0024
0.049	2; 15	6608.3	0.4778	0.7389	2; 25	33.7074	1.00	0.0049
0.066	2; 15	4688.5	0.4613	0.8266	2; 10	56.7074	1.00	0.0125
0.088	2; 15	3041.6	0.5207	0.7114	2; 4	66.1841	1.00	0.0183
0.12	2; 15	1806.3	0.5193	0.5398	2; 8	63.1301	1.00	0.0210
0.15	2; 10	917.25	0.2836	0.4865	2; 15	72.4539	0.99	0.0515
0.21	2; 6	326.66	0.5536	0.7101	2; 8	114.3451	0.91	0.3142
0.37	2; 10	95.84	0.4297	0.5396	2; 20	12.8995	0.99	0.0723
0.49	2; 15	12.06	0.5025	0.6138	2; 25	0.9630	1.00	0.0427
0.66	2; 15	3.03	0.5824	0.5580	2; 15	0.1995	1.00	0.0290
0.88	2; 15	5.65	0.6190	1.4301	2; 10	0.2202	1.00	0.0398
1.17	2; 15	1.43	0.5331	0.8134	2; 8	0.0680	1.00	0.0257
1.56	2; 20	1.44	0.5384	0.8088	2; 8	0.0816	1.00	0.0312
2.08	2; 15	1.84	0.4885	0.9748	2; 8	0.0825	1.00	0.0278
2.77	2; 15	1.02	0.4352	1.0925	1; 4	0.0573	1.00	0.0372
3.70	2; 15	0.52	0.4076	1.0719	1; 8	0.0329	1.00	0.0455
4.92	2; 15	0.28	0.4427	0.9955	1; 4	0.0254	1.00	0.0681
6.56	2; 9	0.11	0.4231	0.9710	1; 6	0.0206	0.99	0.1252
8.75	2; 10	0.060	0.3903	0.9546	2; 6	0.0169	0.98	0.1980
overall	2; 15	2118.577	0.67	1.1324	2; 10	76.6329	0.9989	0.0671

665